U-NO: U-shaped Neural Operators

Anonymous authors
Paper under double-blind review

Abstract

Neural operators generalize classical neural networks to maps between infinite-dimensional spaces, e.g., function spaces. Prior works on neural operators proposed a series of novel methods to learn such maps and demonstrated unprecedented success in learning solution operators of partial differential equations. Due to their close proximity to fully connected architectures, these models mainly suffer from high memory usage and are generally limited to shallow deep learning models. In this paper, we propose U-shaped Neural Operator (*U-NO*), a U-shaped memory enhanced architecture that allows for deeper neural operators. *U-NO*s exploit the problem structures in function predictions and demonstrate fast training, data efficiency, and robustness with respect to hyperparameters choices. We study the performance of *U-NO* on PDE benchmarks, namely, Darcy's flow law and the Navier-Stokes equations. We show that *U-NO* results in an average of 26% and 44% prediction improvement on Darcy's flow and turbulent Navier-Stokes equations, respectively, over the state of art. On Navier-Stokes 3D spatiotemporal operator learning task, we show *U-NO* provides 37% improvement over the state of the art methods.

Keywords: Neural Operators, Partial Differential Equations

1 Introduction

Conventional deep learning research is mainly dominated by neural networks that allow for learning maps between finite dimensional spaces. Such developments have resulted in significant advancements in many practical settings, from vision and nature language processing, to robotics and recommendation systems (Levine et al., 2016; Brown et al., 2020; Simonyan & Zisserman, 2014). Recently, in the field of scientific computing, deep neural networks have been used to great success, particularly in simulating physical systems following differential equations (Mishra & Molinaro, 2020; Brigham, 1988; Chandler & Kerswell, 2013; Long et al., 2015; Chen et al., 2019; Raissi & Karniadakis, 2018). Many real-world problems, however, require learning maps between infinite dimensional functions spaces (Evans, 2010). Neural operators are generalization of neural networks and allow to learn maps between infinite dimensional spaces, including function spaces (Li et al., 2020b). Neural operators are universal approximators of operators and have shown numerous application in tackling problems in partial differential equations (Kovachki et al., 2021b).

Neural operators, in an abstract form, consist of a sequence of linear integral operators, each followed by a nonlinear point-wise operator. Various neural operator architectures have been proposed, most of which focus on the approximation of the Nyström type of the inner linear integral operator of neural operators (Li et al., 2020a;c; Gupta et al., 2021; Tripura & Chakraborty, 2023). For instance, Li et al. (2020a) suggests to use convolution kernel integration and proposes Fourier neural operator (*FNO*), a model that computes the linear integral operation in the Fourier domain. The linear integral operation can also be approximated using discrete wavelet transform (Gupta et al., 2021; Tripura & Chakraborty, 2023). But *FNO* approximates the integration using the fast Fourier transform method (Brigham, 1988) and enjoys desirable approximation theoretic guarantee for continuous operator (Kovachki et al., 2021a). The efficient use of the built-in fast Fourier transform makes the *FNO* approach among the fastest neural operator architectures. Tran et al. (2021) proposes slight modification to the integral operator of *FNO* by factorizing the multidimensional Fourier transform along each dimension. These developments have shown successes in tackling problems in seismology and geophysics, modeling the so-called Digital Twin Earth, and modeling fluid flow in carbon

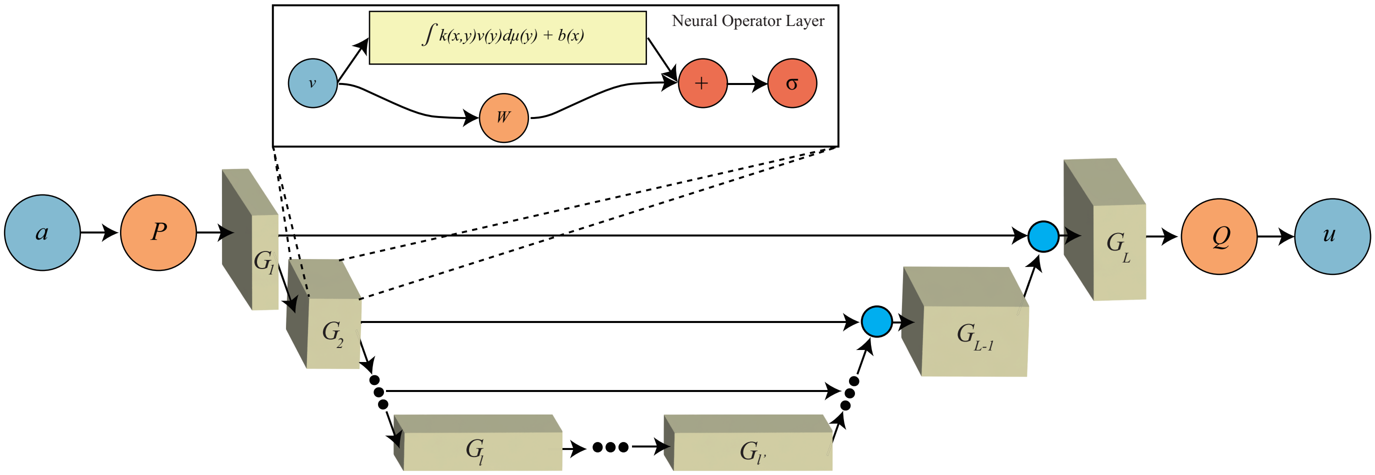

Figure 1: *U-NO* architecture. a is an input function, u is the output. Orange circles are point-wise operators, rectangles denote general operators, and smaller blue circles denote concatenations in function spaces.

capture and storage experiments (Pathak et al., 2022; Yang et al., 2021; Wen et al., 2021; Shui et al., 2020; Li et al., 2022). These are crucial components in dealing with climate change and natural hazards. Many of the initial neural operator architectures are inspired by fully-connected neural networks and result in models with high memory demand that, despite the successes of deep neural networks, prohibit very deep neural operators. Though there are considerable efforts in finding more effective integral operators, works investigating suitable architectures of Neural operators are scarce.

To alleviate this problem, in this paper, we propose the U-shaped Neural Operator (*U-NO*), an architecture that exploits a particular structure of maps between function spaces by progressively transforming the input function space with respect to a sequence of varying domains (see Fig. 1). *U-NO* is inspired by the U-net architectures, an effective model for dealing with finite-dimensional input and output of approximately similar types (Ronneberger et al., 2015). *U-NO*s allow for deeper neural operators, carry information from input to output using skipping pathways between earlier and later layers, and efficiently condense and encode information in function spaces of shrunk domains.

Over the first half of the *U-NO* layers, we map each input function space to vector-valued function spaces with steadily shrunken domains over layers, all the while increasing the dimension of the co-domains, i.e., the output space of each function. Throughout the second half of *U-NO* layers, we gradually expand the domain of each intermediate function space while reducing the dimension of the output function co-domains, and employ skip connections to construct vector-valued functions with larger co-dimension. The gradual contraction of the domain of the input function space in each layer allows for the encoding of function spaces with smaller domains. And the skip connections allow for the direct passage of information at different scales and grids (Long et al., 2015).

The *U-NO* architecture can be adapted to the existing operator learning techniques (Gupta et al., 2021; Tripura & Chakraborty, 2023; Li et al., 2020a; Tran et al., 2021) to achieve a more effective model. In this work, for the implementation of the inner integral operator of *U-NO*, we adopt the Fourier transform-based integration method developed in *FNO*. As *U-NO* contracts the domain of each input function space at the earlier layers, making *U-NO* a memory-efficient architecture, allowing for deeper and highly parameterized neural operators compared with prior works. It is known that over parameterization is one of the main essential components of architecture design in deep learning (He et al., 2016), crucial for performance (Belkin et al., 2019), and optimization (Du et al., 2019). Also recent works show that the model overparameterization improves generalization performance (Neyshabur et al., 2017; Zhang et al., 2021; Dar et al., 2021). The *U-NO* architecture allows efficient training of overparameterized model with smaller memory footprint and opens neural operator learning to deeper and highly parameterized methods.

We establish our empirical study on Darcy's flow and the Navier-Stokes equations, two PDEs which have served as benchmarks for the study of neural operator models. We compare the performance of *U-NO* against the state of art *FNO*. We empirically show that the advanced structure of *U-NO* allows for much deeper neural operator models with smaller memory usage. We demonstrate that *U-NO* achieves average performance improvements of **26%** on high resolution simulations of Darcy's flow equation, and **44%** on Navier-Stokes equation, with the best improvement of **51%**. On Navier-Stokes 3D spatio-temporal operator learning task, for which the input functions are defined on the $3D$ spatio-temporal domain, we show *U-NO* provides **37%** improvement over the state of art *FNO* model. Also, the *U-NO* outperforms the baseline *FNO* on zero-shot super resolution experiment.

It is important to note that *U-NO* is the first neural operator trained for mapping from function spaces with 3D domains. Prior studies on 3D domains either transform the input function space with the 3D spatio-temporal domain to another auxiliary function space with 2D domain for the training purposes, resulting in an operator that is time discretization dependent or modifies the input function by extending the domain and co-domain (Li et al., 2020a). We further show that *U-NO* allows for much deeper models ($3\times$) with far more parameters ($25\times$), while still providing some performance improvement (Appendix A.2). Such a model can be trained with only a few thousand data points, emphasizing the data efficiency of problem-specific neural operator architecture design.

Moreover, we empirically study the sensitivity of *U-NO* against hyperparameters (Appendix A.2) where we demonstrate the superiority of this model against *FNO*. We observe that *U-NO* is much faster to train (Appendix A.6)and also much easier to tune. Furthermore, for *U-NO* as a model that gradually contracts (expands) the domain (co-domain) of function spaces, we study its variant which applies these transformations more aggressively. A detailed empirical analysis of such variant of *U-NO* shows that the architecture is quite robust with respect to domain/co-domain transformation hyperparameters.

2 Neural Operator Learning

Let $\mathcal{A}$ and $\mathcal{U}$ denote input and output function spaces, such that, for any vector valued function $a \in \mathcal{A}$, $a : \mathcal{D}_{\mathcal{A}} \to \mathbb{R}^{d_{\mathcal{A}}}$, with $\mathcal{D}_{\mathcal{A}} \subset \mathbb{R}^d$ and for any vector valued function $u \in \mathcal{U}$, $u : \mathcal{D}_{\mathcal{A}} \to \mathbb{R}^{d_{\mathcal{U}}}$, with $\mathcal{D}_{\mathcal{U}} \subset \mathbb{R}^d$. Given a set of N data points, $\{(a_j, u_j)\}_{j=1}^N$, we aim to train a neural operator $\mathcal{G}_\theta : \mathcal{A} \to \mathcal{U}$, parameterized by θ, to learn the underlying map from a to u. Neural operators, in an abstract sense, are mainly constructed using a sequence of non-linear operators G_i that are linear integral operators followed by point-wise non-linearity, i.e., for an input function v_i at the ith layer, $G_i : v_i \to v_{i+1}$ is computed as follows,

$$G_i v_i(x) := \sigma\Big(\int \kappa_i(x, y) v_i d\mu_i(y) + W_i v_i(x) \Big) \tag{1}$$

Here, κ_i is a kernel function that acts, together with the integral, as a global linear operator with measure μ_i, W_i is a matrix that acts as a point-wise operator, and σ is the point-wise non-linearity. One can explicitly add a bias function b_i separately. Together, these operations constitute G_i, i.e., a nonlinear operator between a function space of d_i dimensional vector-valued functions with the domain $\mathcal{D}_i \subset \mathbb{R}^d$ and a function space of d_{i+1} dimensional vector-valued functions with the domain $\mathcal{D}_{i+1} \subset \mathbb{R}^d$. Neural operators often times are accompanied with a point-wise operator P that constitute the first block of the neural operator and mainly serves as a lifting operator directly applied to input function, and a point-wise operator Q, for the last block, that is mainly purposed as a projection operator to the output function space.

Previous deployments of neural operators have studied settings in which the domains and co-domains of function spaces are preserved throughout the layers, i.e., $\mathcal{D} = \mathcal{D}_i = \mathcal{D}_{i+1}$, and $d' = d_i = d_{i+1}$, for all i. These models, e.g. *FNO*, impose that each layer is a map between functions spaces with identical domain and co-domain spaces. Therefore, at any layer i, the input function is $\nu_i : \mathcal{D} \to \mathbb{R}^{d'}$ and the output function is $\nu_{i+1} : \mathcal{D} \to \mathbb{R}^{d'}$, defined on the same domain $\mathcal{D}$ and co-domain $\mathbb{R}^{d'}$. This is one of the main reasons for the high memory demands of previous implementations of neural operators, which occurs primarily from the global integration step. In this work, we avoid this problem, since as we move to the innermost layers of the neural operator, we contract the domain of each layer while increasing the dimension of co-domains. As a result we sequentially encode the input functions into functions with smaller domain, learning compact representation as well as resulting in integral operations in much smaller domains.

3 A U-shaped Neural Operator (*U-NO*)

In this section, we introduce the *U-NO* architecture, which is composed of several standard elements from prior works on Neural Operators, along with U-shaped additions tailored to the structure of function spaces (and maps between them). Given an input function $a : \mathcal{D}_\mathcal{A} \to \mathbb{R}^{d_\mathcal{A}}$, we first apply a point-wise operator P to a and compute $v_0 : \mathcal{D}_\mathcal{A} \to \mathbb{R}^{d_0}$. The point-wise operator P is parameterized with a function $P_\theta : \mathbb{R}^{d_\mathcal{A}} \to \mathbb{R}^{d_0}$ and acts as

$$v_0(x) = P_\theta(a(x)),\ \forall x \in \mathcal{D}_0$$

where $\mathcal{D}_0 = \mathcal{D}_\mathcal{A}$. The function P_θ can be matrix or more generally a deep neural network. For the purpose of this paper, we take $d_0 \gg d_\mathcal{A}$, making P a lifting operator.

Then a sequence of L_1 non-linear integral operators is applied to v_0,

$$\mathcal{G}_i : \{v_i : \mathcal{D}_i \to \mathbb{R}^{d_{v_i}}\} \to \{v_{i+1} : \mathcal{D}_{i+1} \to \mathbb{R}^{d_{v_i+1}}\} \quad \text{for } i \in \{0, 1, 2 \ldots L_1\},$$

where for each i, $\mathcal{D}_i \subset \mathbb{R}^d$ is a measurable set accompanied by a measure μ_i. Application of this sequence of operators results in a sequence of intermediate functions $\{v_i : \mathcal{D}_i \to \mathbb{R}^{d_{v_i}}\}_{i=1}^{L_1+1}$ in the encoding part of *U-NO*.

In this study, without loss of generality, we choose Lebesgue measure μ for μ_i's. Over this first L_1 layers, i.e., the encoding half of *U-NO*, we map the input function to a set of vector-valued functions with increasingly contracted domain and higher dimensional co-domain, i.e. for each i, we have $\mu(D_i) \geq \mu(D_{i+1})$ and $d_{v_{i+1}} \geq d_{v_i}$.

Then, given v_{L_1+1}, another sequence of L_2 non-linear integral operator layers (i.e. the decoder), is applied. In this stage, the operators gradually expand the domain size and decrease the co-domain dimension to ultimately match the domain of the terget function, i.e., for each i in these layers, we have $\mu(D_{i+1}) \geq \mu(D_i)$ and $d_{v_i} \geq d_{v_{i+1}}$.

To include the skip connections from the encoder part from the encoder part to the decoder in (see Fig. 1), the operator G_{L_1+i} in the decoder part, takes a vector-wise concatenation of both v_{L_1+i} and v_{L_1-i} as its input. The vector-wise concatenation of v_{L_1+i} and v_{L_1-i} is a function v'_{L_1+i} where,

$$v'_{L_1+i} : \mathcal{D}_{L_1+i} \to \mathbb{R}^{d_{(L_1-i)}+d_{(L_1+i)}} \text{ and } v'_{L_1+i}(x) = \left[v_{L_1-i}(x)^\top, v_{L_1+i}(x)^\top\right]^\top,\ \forall x \in \mathcal{D}_{L_1+i}.$$

v'_{L_1+i} constitutes the input to the operator G_{L_1+i}, and we compute the output function of the next layer as,

$$v_{(L_1+i)+1} = \mathcal{G}_{i+L_1} v'_{i+L_1}.$$

Here, for simplicity, we assumed $D_{L_1+i} = D_{L_1-i}$[1].

Computing v_{L+1} for the layer $L = L_1 + L_2$, we conclude *U-NO* architecture with another point-wise operator Q kernelized with the $Q_\theta : \mathbb{R}^{d_{L+1}} \to \mathbb{R}^{d_\mathcal{U}}$ such that for $u = Qv_{L+1}$ we have

$$u(x) = Q_\theta(v_{L+1}(x)), \forall x \in \mathcal{D}_{L+1}$$

where $D_{L+1} = D_\mathcal{U}$. In this paper we choose $d_{L+1} \gg d_\mathcal{U}$ such that Q is a projection operator. In the next section, we instantiate the *U-NO* architecture for two benchmark operator learning tasks.

4 Empirical Studies

In this section, we describe the problem settings, implementations, and the empirical results.

[1] More generally, concatenation can be defined with a map between the domains $m : D_{L_1+i} \to D_{L_1-i}$ as $v'_{i+L_1}(x) = \left[v_{L_1-i}\big(m(x)\big), v_{L_1+i}\big(x\big)\right]^\top$

4.1 Darcy Flow Equation

The 2-d Darcy Flow is a second-order linear elliptic equation with a Dirichlet boundary of the following form,

$$\begin{aligned} -\nabla \cdot (a(x)\nabla u(x)) &= f(x) & x \in D \\ u(x) &= 0 & x \in \partial D \end{aligned}$$

where $a \in \mathcal{A} \subseteq L^\infty(D;\mathbb{R}_+), u \in \mathcal{U} \subseteq H_0^1(D;\mathbb{R})$ and $f \in \mathcal{F} = H^{-1}(D;\mathbb{R})$. Here, a is the diffusion coefficients and f is the forcing function. We take $D = (0,1)^2$ and aim to learn the solution operator $G^\dagger$ which maps a diffusion coefficient function a to the solution u, i.e., $u = G^\dagger(a)$.

For dataset preparation, we define $\mu = \psi_{\#}\mathcal{N}(0,(-\Delta + 9I)^{-2})$ as a probability measure with zero Neumann boundary conditions on the Laplacian where $\forall x \geq 0,\ \psi(x) = 12$ and $\forall x < 0,\ \psi(x) = 3$. The diffusion coefficients $a(x)$ are generated according to $a \sim \mu$ and we fix $f(x) = 1$. The solutions are obtained by using a second-order finite difference method on a uniform 421×421 grid over $(0,1)^2$. And solutions of any other resolution are down-sampled from the high resolution data. This set up is the same benchmark set up in the prior works.

4.2 Navier-Stokes Equation

The vorticity-streamfunction formulation of the 2-d Navier-Stokes equations for a viscous and incompressible fluid on the unit torus ($\mathbb{T}^2$) is given by,

$$\begin{aligned} \partial_t w(x,t) + \nabla^\perp \psi \cdot \nabla w(x,t) &= \nu \Delta w(x,t) + g(x), & x \in \mathbb{T}^2, t \in (0,\infty), \\ -\Delta \psi &= \omega, & x \in \mathbb{T}^2, t \in (0,\infty), \\ w(x,0) &= w_0(x), & x \in \mathbb{T}^2, \end{aligned}$$

where, $w = \nabla \times u$ is the vorticity field and $w_0 \in L^2_{\text{per}}((0,1)^2;\mathbb{R})$ is the initial vorticity field. Here $u \in \mathcal{U} = C\big([0,T]; H^r_{\text{per}}((0,1)^2;\mathbb{R}^2)\big)$ is the velocity field, where H^r_{per} is the periodic Sobolev space H^r with constant $r \geq 0$. The stream function ψ is related to velocity by $u = \nabla^\perp \psi$. The function g is defined as the curl of the forcing function, f, i.e. $g := (\Delta \times f) \in L^2_{\text{per}}((0,1)^2;\mathbb{R})$, and $\nu \in \mathbb{R}_+$ is the viscosity coefficient.

Following Kovachki et al. (2021b), we generated the vorticity w_0 as ($w_0 \sim \mathcal{N}(0, 7^{3/2}(-\Delta + 49I)^{-5/2})$ with periodic boundary condition. We fix g, the curl of the forcing function, as

$$g(x_1,x_2) = 0.1\big(\sin(2\pi(x_1+x_2)) + \cos(2\pi(x_1+x_2))\big),\ \forall (x_1,x_2) \in \mathbb{T}^2$$

The equation is solved using the pseudo-spectral split step method. The forcing terms are advanced using Heun's method and the viscous terms are advanced using a Crank–Nicolson update with time-step of 10^{-4}. We record the solution every $t = 1$ time units. The data is generated on a uniform 256×256 grid and are downsampled to 64×64 for the low resolution training.

For this time dependent problem, we aim to learn an operator that maps the vorticity field covering a time interval spanning $[0, T_{in}]$, into the vorticity field for a later time interval, $(T_{in}, T]$,

$$G^\dagger : C([0,T_{in}]; H^r_{\text{per}}((0,1)^2;\mathbb{R})) \to C((T_{in},T]; H^r_{\text{per}}((0,1)^2;\mathbb{R}))$$

In terms of vorticity, the operator is defined by $w|_{(0,1)^2 \times [0,T_{in}]} \to w|_{(0,1)^2 \times (T_{in},T]}$.

4.3 Model Implementation

We present the specific implementation of the models used for our experiments discussed in the remainder of this section. For the internal integral operators, we adopt the approach of Li et al. (2020a), in which, evoking convolution theorem, the integral kernel (convolution) operators are computed by the multiplication of Fourier transform of kernel convolution operators and the input function in the Fourier domain. Such operation is approximately computed using fast Fourier transform, providing computational benefit compared to the other Nyström integral approximation methods developed in neural operator literature, and additional performance benefits results from computing the kernels directly in the Fourier domain, evoking the spectral convergence (Canuto et al., 2007). Therefore, for a given function v_i, i.e., the input to the G_i, we have,

$$G_i v_i(x) = \sigma\Big(\mathcal{F}^{-1}\big(R_i \cdot \mathcal{F}(v_i)\big)(x) + W_i v_i(x)\Big)$$

Here $\mathcal{F}$ and $\mathcal{F}^{-1}$ are the Fourier and Inverse Fourier transforms, respectively. $R_i : \mathbb{Z}^d \to \mathbb{C}^{d_{i+1}\times d_i}$, and for each Fourier mode $k \in \mathbb{Z}^d$, it is the Fourier transform of the periodic convolution function in the integral convolution operator. We directly parameterize the matrix valued functions R_i on $\mathbb{Z}^d$ in the Fourier domain and learn it from data. For each layer i, we also truncate the Fourier series at a preset number of modes,

$$k^i_{max} = |Z^i_{k_{max}}| = |k \in \mathbb{Z}^d : k_j \leq k^i_{max,j} \text{ for } j \in \{1, \dots d\}|.$$

Thus, R_i is implicitly a complex valued $(k^i_{max} \times d_{v_{i+1}} \times d_{v_i})$ tensor. Assuming the discretization of the domain is regular, this non-linear operator is implemented efficiently with the fast Fourier transform. Finally, we define the point-wise residual operation $W_i v_i$ where

$$W_i v_i(x) = W_i v_i\left((s(x)\right)$$

with $x \in \mathcal{D}_{i+1}$ and $s : \mathcal{D}_{i+1} \to \mathcal{D}_i$ is a fixed homeomorphism between $\mathcal{D}_{i+1}$ and $\mathcal{D}_i$.

In the empirical study, we need two classes of operators. The first one is an operator setting where the input and output functions are defined on 2D spatial domain. And in the second setting, the input and output are defined on 3D spatio temporal setting. In the following, we describe the architecture of *U-NO* for both of these settings.

Operator learning on functions defined on 2D spatial domains. For mapping between functions defined on $2D$ spatial domain, the solution operator is of form $G^\dagger : \{a : (0,1)^2 \to \mathbb{R}^{d_\mathcal{A}}\} \to \{u : (0,1)^2 \to \mathbb{R}^{d_\mathcal{U}}\}$. The *U-NO* architecture consists of a series of seven non-linear integral operators, $\big\{G_i\big\}_{i=0}^{7}$, that are placed between lifting and projection operators. Each layer performs a 2D integral operation in the spatial domain and contract (or expand) the spatial domain (see Fig. 1).

The first non-linear operator, G_0, contracts the domain by a factor of $\frac{3}{4}$ uniformly along each dimension, while increasing the dimension of the co-domain by a factor of $\frac{3}{2}$,

$$G_0 : \{v_0 : (0,1)^2 \to \mathbb{R}^{d_{v_0}}\} \to \{v_1 : \big(0, 3/4\big)^2 \to \mathbb{R}^{\lceil \frac{3}{2} d_{v_0} \rceil}\}.$$

Similarly, G_1 and G_2 sequentially contract the domain by a factor of $\frac{2}{3}$ and $\frac{1}{2}$, respectively, while doubling the dimension of the co-domain. G_3 is a regular Fourier operator layer and thus the domain or co-domain of its input and out function spaces stay the same. The last three Fourier operators, $\big\{G_i\big\}_{i=4}^{6}$, expand the domain and decrease the co-domain dimension, restoring the domain and co-domain to that of the input to G_0.

We further propose *U-NO*† which follows a more aggressive factor of $\frac{1}{2}$ (shown in Fig. 2A) while contracting (or expanding) the domain in each of the integral operators. One of the reasons for this choice is that such a selection of scaling factors is more memory efficient than the initial *U-NO* architecture.

The projection operator Q and lifting operator P are implemented as fully-connected neural networks with lifting dimension $d_0 = 32$. And we set skip connections from the first three integral operator (G_0, G_1, G_2) respectively to the last three (G_6, G_5, G_4).

For time dependent problems, where we need to map between input functions a of an initial time interval $[0, T_{in}]$, to the solution functions u of later time interval $(T_{in}, T]$, i.e., to learn an operator of form,

$$G^\dagger : C\big([0, T_{in}], \{a : (0,1)^2 \to \mathbb{R}^{d_\mathcal{A}}\}\big) \to C\big(\{(T_{in}, T], u : (0,1)^2 \to \mathbb{R}^{d_\mathcal{U}}\}\big)$$

we use an auto regressive model for *U-NO* and *U-NO*†. Here recurrently compose the neural operator in time to produce solution functions for the time interval $(T_{in}, T]$.

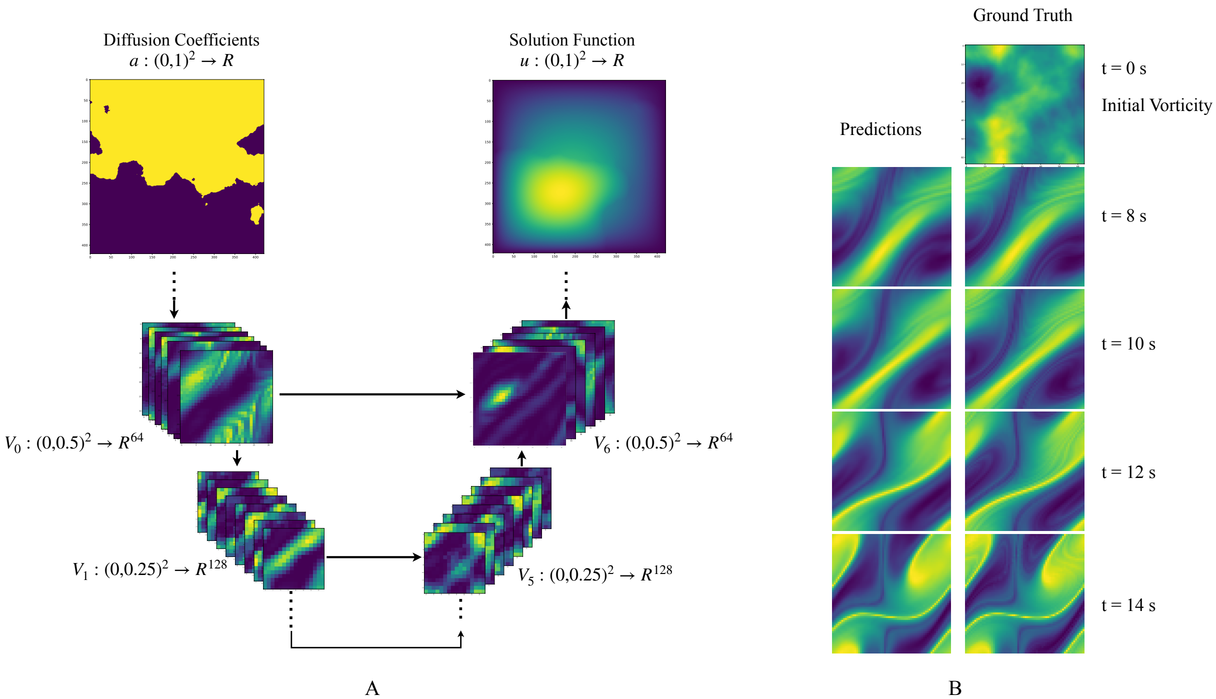

Figure 2: (A) An illustration of aggressive contraction and re-expansion of the domain (and vice versa for the co-domains) by the variant of *U-NO* with a factor of $\frac{1}{2}$ on an instance of Darcy flow equation. (B) Vorticity field generated by the *U-NO* variant as a solution to an instance of the two-dimensional Navier-Stokes equation with viscosity 10^{-6}.

Operator learning on functions defined on 3D spatio-temporal domains. Separately, we also use a *U-NO* model with non-linear operators that performs the integral operation in space and time ($3D$), which directly maps the input functions a of interval $[0, T_{in}]$ to the later time interval $(T_{in}, T]$, without any recurrent composition in time. As this model does not require recurrent composition in time, it is fast during both training and inference. We redefine both a and u on $3D$ spatio-temporal domain and learn the the operator

$$G^\dagger : \{a : (0,1)^2 \times [0, T_{in}] \to \mathbb{R}^{d_\mathcal{A}}\} \to \{u : (0,1)^2 \times (T_{in}, T] \to \mathbb{R}^{d_\mathcal{U}}\}$$

The non-linear operators constructing *U-NO*, $\{G_i\}_{i=0}^{L}$, are defined as,

$$G_i : \{v_i : (0, \alpha_i)^2 \times \mathcal{T}_i \to \mathbb{R}^{d_{v_0}}\} \to \{v_{i+1} : \big(0, c_i^s \alpha_i\big)^2 \times (T_{in}, T_{in} + c_i^t T_{in}] \to \mathbb{R}^{c_i^c d_{v_0}}\}.$$

Here, $(0, \alpha_i)^2 \times \mathcal{T}_i$ is the domain of the function v_i. And c_i^s, c_i^t and c_i^c are respectively the expansion (or contraction) factors for spatial domain, temporal domain, and co-domain for i'th operator. Note that $\mathcal{T}_0 = [0, T_{in}]$, $(0,\alpha_0) = (0, \alpha_{L+1}) = (0, 1)$, and $\mathcal{T}_{L+1} = (T_{in}, T]$.

Here we also first contract and then expand (i.e., $c_i^s \leq 1$ in the encoding part and $c_i^s \geq 1$ in the decoding part) the spatial domain following the *U-NO* performing $2D$ integral operation. And we set $c_i^t \geq 1$ for all operators G_i if the output time interval is larger than input time interval i.e. $T_{in} < T_{out} - T_{in}$ i.e., we gradually increase the time domain of the input function to match the output. Here the projection operator Q and lifting operator P are also implemented as fully connected neural network with $d_0 = 8$ for the lifting operator P.

For the experiments, we use Adam optimizer (Kingma & Ba, 2014) and the initial learning rate is scaled down by a factor of 0.5 every 100 epochs. As the non-linearity, we have used the GELU (Hendrycks & Gimpel, 2016) activation function. All the computation are carried on a single Nvidia GPU with 24GB memory. For each experiments the data is divided into train, test, and validation set. And weight of the best performing model on the validation set is used for evaluation. Each experiment is repearted 3 times and the mean is reported.

In the following, we empirically study the performance of these models on Darcy Flow and Navier-Stokes Equations.

4.4 Results on Darcy Flow Equation

From the dataset of $N = 2000$ simulations of the Darcy flow equation, we set aside 250 simulations for testing and use the rest for training and validation. We use *U-NO*† with 9 layers including the integral, lifting, and projection operators . We train for 700 epochs and save the best performing model on the validation set for evaluation. The performances of *U-NO*† and *FNO* on several different grid resolutions are shown in Table. 1. The number of modes used in each integral operator stays unchanged throughout different resolutions. We demonstrate that *U-NO*† achieve lower relative error on every resolution with **27%** improvement on high resolution (421×421) simulations. The U-shaped structure exploits the problem structure and gradually encodes the input function to functions with smaller domains, which enables *U-NO*† to have efficient deep architectures, modeling complex non-linear mapping between the input and solution function spaces. We also notice that *U-NO*† requires **23%** less training memory while having **7.5** times more parameters. With vanilla FNO, designing such over paramterized deep operator to learn complex maps is impracticable due to high memory requirements.

Table 1: Benchmarks on Darcy Flow. The average relative error in percentage is reported with error bars are indicated in the superscript. The average back-propagation memory requirements for a single training instance is reported over different resolutions are reported. *U-NO*† performs better than *FNO* for every resolution, while requiring 23% lower training memory which allows efficient training of 7.5 times more parameters

Model	**Mem. Req.** (MB)	**# Parameter** $\times 10^6$	**Resolution** $s \times s$ s = 421	s = 211	s = 141	s = 85
U-NO†	**166**	8.2	$0.57^{\pm\mathbf{1.4e-2}}$	$0.58^{\pm\mathbf{0.4e-2}}$	$0.60^{\pm\mathbf{0.5e-2}}$	$0.73^{\pm\mathbf{0.1e-2}}$
FNO	214	1.1	$0.78^{\pm\mathbf{4.0e-2}}$	$0.84^{\pm\mathbf{5.5e-2}}$	$0.84^{\pm\mathbf{1.1e-2}}$	$0.87^{\pm\mathbf{3.0e-2}}$

Table 2: Zero-shot super resolution result on Darcy Flow. Neural operators trained on lower spatial resolution data is directly tested on higher resolution with no further training. We observe *U-NO*† archives lower percentage relative error rate.

	Train \ Test	s = 141	s = 211	s = 421
U-NO†	s=85	4.7	6.2	8.3
	s=141	-	2.6	6.3
	s=211	-	-	4.5
FNO	s=85	7.5	14.1	23.9
	s=141	-	4.3	13.1
	s=211	-	-	9.6

4.5 Results on Navier-Stokes Equation

For the auto-regressive model, we follow the architecture for *U-NO* and *U-NO*† described in Sec. 4.3. For *U-NO* performing spatio-temporal ($3D$) integral operation, we use 7 stacked non-linear integral operator following the same spatial contracting and expansion of 2D spatial *U-NO*. Additionally, as the positional embedding for the domain (unit torus $\mathbb{T}^2$) we used the Clifford torus (Appendix A.1) which embeds the domain into Euclidean space. It is important to note that, for spatio-temporal *FNO* setting, the domain of

Table 3: Benchmarks on Navier-Stokes. For the models performing a $2D$ integral operator with recurrent structure in time, back-propagation memory requirement per time step is reported. *U-NO* yields superior performance compared with *U-NO*† and *FNO*, while *U-NO*† is the most memory efficient model. In the $3D$ integration setting, *U-NO* provides significant performance improvement with almost three times less memory requirement.

model		**Avg. Mem. Req.** (MB)	**# Parameters** ($\times 10^6$)	$\nu = $ 1e$-$3, $T = 50s$, $T_{in} = 10s$, $N = 5000$	$\nu = $ 1e$-$4, $T = 30s$, $T_{in} = 10s$, $N = 11000$	$\nu = $ 1e$-$5, $T = 20s$, $T_{in} = 10s$, $N = 11000$	$\nu = $ 1e$-$6, $T = 15s$, $T_{in} = 6$s, $N = 11000$
$2D$	*U-NO*	16	15.3	$0.28^{\pm \mathbf{2.1e-2}}$	$3.44^{\pm \mathbf{6.3e-2}}$	$2.94^{\pm \mathbf{4.9e-2}}$	$1.76^{\pm \mathbf{1.4e-2}}$
	U-NO†	**11**	6.7	$0.35^{\pm \mathbf{2.0e-2}}$	$3.56^{\pm \mathbf{4.3e-2}}$	$3.60^{\pm \mathbf{1.2e-2}}$	$2.2^{\pm \mathbf{1.5e-2}}$
	FNO	13	1.3	$0.58^{\pm \mathbf{1.4e-2}}$	$5.57^{\pm \mathbf{7.7e-2}}$	$5.12^{\pm \mathbf{0.7e-2}}$	$3.33^{\pm \mathbf{0.7e-2}}$
$3D$	*U-NO*	**108**	24.0	$0.31^{\pm \mathbf{3.9e-2}}$	$5.59^{\pm \mathbf{2.9e-1}}$	$7.03^{\pm \mathbf{4.6e-2}}$	$5.10^{\pm \mathbf{1.0e-1}}$
	FNO	216	1.3	$0.68^{\pm \mathbf{0.8e-2}}$	$9.60^{\pm \mathbf{5.4e-2}}$	$8.67^{\pm \mathbf{1.2e-1}}$	$7.35^{\pm \mathbf{6.3e-1}}$

the input function is extended to match the solution function as it maps between the function spaces with same domains. Capable of mapping between function spaces with different domains, no such modification is required for *U-NO*.

For each experiment, 10% of the total number of simulations N are set aside for testing, and the rest is used for training and validation. We experiment with the viscosity as $\nu \in \{$1e-3, 1e-4, 1e-5, 1e$-6\}$, adjusting the final time T as the flow becomes more chaotic with smaller viscosities.

Table 3 demonstrates the results of the Navier-Stokes experiment. We observe that *U-NO* achieves the best performance, with nearly a **50%** reduction in the relative error over *FNO* in some experimental settings; it even achieves nearly a **1.76%** relative error on a problem with a Reynolds number[2] of 2×10^4 (Fig. 2B). In each case, the *U-NO*† with aggressive contraction (and expansion) factor, performs significantly better than *FNO*–while requiring less memory. Also for neural operators performing $3D$ integral operation, *U-NO* achieved **37%** lower relative error while requiring **50%** less memory on average with **19** times more parameters and unlike *FNO* it is able to perform zero-shot super resolution in both time and spacial domain (Appendix A.5).

Table 4: Related Error (%) achieved by 2D *U-NO* and 3D *U-NO* trained and evaluated on high resolution (256×256) Simulations of Navier-Stokes. Even with highly constrained neural operator architecture and smaller training data, the *U-NO* architecture can achieve comparable performance.

Models *U-NO*	**Memory Requirement** (MB)	$\nu = $ 1e$-$3, $N = 2400$	$\nu = $ 1e$-$4, $N = 6000$	$\nu = $ 1e$-$5, $N = 6000$	$\nu = $ 1e$-$6, $N = 6000$
$2D$ *U-NO*	86	0.51	5.9	7.0	4.4
$3D$ *U-NO*	850	0.83	8.3	11.2	8.2

Due to U-shaped encoding decoding structure–which allow us to train *U-NO* on very high resolution (256×256) data on a single GPU with a $24GB$ memory. To accommodate training with high-resolution simulations of the Navier-Stocks equation, we have adjusted the contraction (or expansion) factors. The Operators in the encoder part of *U-NO* follow a contraction ratio of $\frac{1}{4}$ and $\frac{1}{2}$ for the spatial domain. But the co-domain dimension is increased only by a factor of 2. And the operators in the decoder part follow the reciprocals of these ratios. We have also used a smaller lifting dimension for the lifting operator P. Even with such a compact architecture and lower training data, *U-NO* achieves lower error rate on high resolution data

[2] Reynolds number is estimated as $Re = \frac{\sqrt{0.1}}{\nu (2\pi)^{(3/2)}}$ (Chandler & Kerswell, 2013)

(Table 4). These gains are attributed to the deeper architecture, skip connections, and encoding/decoding components of *U-NO*.

4.6 Remarks on Memory Usage

Compared to *FNO*, the proposed *U-NO* architectures consume less memory during training and testing. Due to the gradual encoding of input function by contracting the domain, the *U-NO* allow for deeper architectures with a greater number of stacked non-linear operators and higher resolution training data (Appendix A.4). For *U-NO*, an increase in depth, does not significantly raise the memory requirement. The training memory requirement for 3D spatio-temporal *U-NO* and *FNO* is reported in Fig. 3A.

We can observe a linear increase in memory requirement for *FNO* with the increase of depth. This makes *FNO* s unsuitable for designing and training very deep architectures as the memory requirement keep increasing rapidly with the increase of the depth. On the other hand, due to the repeated scaling of the domain, we do not observe any significant increase in the memory requirement for *U-NO*. This make the *U-NO* a suitable architecture for designing deep neural operators. The improvement of the performance with the increase of

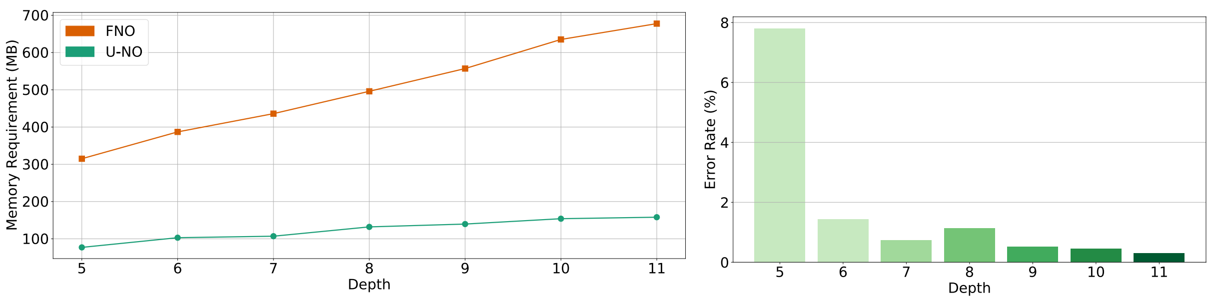

A B

Figure 3: (A) Training memory requirements (in MB) for the 3D spatio-temporal problem of Navier-Stokes equation ($\nu = 1\text{e}{-3}$). For different depth only the number of stacked non-linear operators is varied. For deeper models, the additive memory requirement of *U-NO* is negligible compared to *FNO* model. For addition of 7 more integral layer memory requirement only increased by only **80MB** (vs $\sim$ **400MB** for *FNO*). (B) Relative error in percentage on 3D spatio-temporal Navier-Stokes equation ($\nu = 1\text{e}{-3}$) for different depth (average over three repeated experiment is reported). We can observe a gradual decrease in the relative error with the increase of depth.

depth is shown in Fig. 3B. This is expected as highly parameterized deep architectures allow for effective approximation of highly complex non-linear operators. *U-NO* style architectures are more favorable for learning complex maps between function spaces.

5 Conclusion

In this paper, we propose *U-NO*, a new neural operator architecture with a multitude of advantages as compared with prior works. Our approach is inspired by *Unet*, a neural network architecture that is highly successful at learning maps between finite-dimensional spaces with similar structures, e.g., image to image translation. *U-NO* possesses a similar set of benefits to *Unet*, including data efficiency, robustness to hyperparameter tuning (Appendix A.2), flexible training, memory efficiency, convergence (Appendix A.6), and non-vanishing gradients.This approach, while advancing neural operator research, significantly improves the performance and learning paradigm, still carries the fundamental and inherent memory usage limitation of integral operators. Nevertheless, *U-NO* allows for much deeper models incorporating the problem structures and provides highly parameterized neural operators for learning maps between function spaces. *U-NO*s are very easy to tune, possess faster convergence to desired accuracies, and achieve superior performance with minimal tuning.

References

Mikhail Belkin, Daniel Hsu, Siyuan Ma, and Soumik Mandal. Reconciling modern machine-learning practice and the classical bias–variance trade-off. *Proceedings of the National Academy of Sciences*, 116(32): 15849–15854, 2019.

E Oran Brigham. *The fast Fourier transform and its applications.* Prentice-Hall, Inc., 1988.

Tom Brown, Benjamin Mann, Nick Ryder, Melanie Subbiah, Jared D Kaplan, Prafulla Dhariwal, Arvind Neelakantan, Pranav Shyam, Girish Sastry, Amanda Askell, et al. Language models are few-shot learners. *Advances in neural information processing systems*, 33:1877–1901, 2020.

Claudio Canuto, M Yousuff Hussaini, Alfio Quarteroni, and Thomas A Zang. *Spectral methods: fundamentals in single domains.* Springer Science & Business Media, 2007.

Gary J Chandler and Rich R Kerswell. Invariant recurrent solutions embedded in a turbulent two-dimensional kolmogorov flow. *Journal of Fluid Mechanics*, 722:554–595, 2013.

Zhengdao Chen, Jianyu Zhang, Martin Arjovsky, and Léon Bottou. Symplectic recurrent neural networks. *arXiv preprint arXiv:1909.13334*, 2019.

Yehuda Dar, Vidya Muthukumar, and Richard G Baraniuk. A farewell to the bias-variance tradeoff? an overview of the theory of overparameterized machine learning. *arXiv preprint arXiv:2109.02355*, 2021.

Simon Du, Jason Lee, Haochuan Li, Liwei Wang, and Xiyu Zhai. Gradient descent finds global minima of deep neural networks. In *International conference on machine learning*, pp. 1675–1685. PMLR, 2019.

Lawrence C Evans. *Partial differential equations*, volume 19. American Mathematical Soc., 2010.

Gaurav Gupta, Xiongye Xiao, and Paul Bogdan. Multiwavelet-based operator learning for differential equations. *Advances in Neural Information Processing Systems*, 34, 2021.

Kaiming He, Xiangyu Zhang, Shaoqing Ren, and Jian Sun. Deep residual learning for image recognition. In *Proceedings of the IEEE conference on computer vision and pattern recognition*, pp. 770–778, 2016.

Dan Hendrycks and Kevin Gimpel. Gaussian error linear units (gelus). *arXiv preprint arXiv:1606.08415*, 2016.

Diederik P Kingma and Jimmy Ba. Adam: A method for stochastic optimization. *arXiv preprint arXiv:1412.6980*, 2014.

Nikola Kovachki, Samuel Lanthaler, and Siddhartha Mishra. On universal approximation and error bounds for fourier neural operators. *Journal of Machine Learning Research*, 22:Art–No, 2021a.

Nikola Kovachki, Zongyi Li, Burigede Liu, Kamyar Azizzadenesheli, Kaushik Bhattacharya, Andrew Stuart, and Anima Anandkumar. Neural operator: Learning maps between function spaces. *arXiv preprint arXiv:2108.08481*, 2021b.

Sergey Levine, Chelsea Finn, Trevor Darrell, and Pieter Abbeel. End-to-end training of deep visuomotor policies. *The Journal of Machine Learning Research*, 17(1):1334–1373, 2016.

Bian Li, Hanchen Wang, Xiu Yang, and Youzuo Lin. Solving seismic wave equations on variable velocity models with fourier neural operator. *arXiv preprint arXiv:2209.12340*, 2022.

Zongyi Li, Nikola Kovachki, Kamyar Azizzadenesheli, Burigede Liu, Kaushik Bhattacharya, Andrew Stuart, and Anima Anandkumar. Fourier neural operator for parametric partial differential equations. *arXiv preprint arXiv:2010.08895*, 2020a.

Zongyi Li, Nikola Kovachki, Kamyar Azizzadenesheli, Burigede Liu, Kaushik Bhattacharya, Andrew Stuart, and Anima Anandkumar. Neural operator: Graph kernel network for partial differential equations. *arXiv preprint arXiv:2003.03485*, 2020b.

Zongyi Li, Nikola Kovachki, Kamyar Azizzadenesheli, Burigede Liu, Andrew Stuart, Kaushik Bhattacharya, and Anima Anandkumar. Multipole graph neural operator for parametric partial differential equations. *Advances in Neural Information Processing Systems*, 33, 2020c.

Jonathan Long, Evan Shelhamer, and Trevor Darrell. Fully convolutional networks for semantic segmentation. In *Proceedings of the IEEE conference on computer vision and pattern recognition*, pp. 3431–3440, 2015.

Siddhartha Mishra and Roberto Molinaro. Estimates on the generalization error of physics informed neural networks (pinns) for approximating a class of inverse problems for pdes. *arXiv preprint arXiv:2007.01138*, 2020.

Behnam Neyshabur, Srinadh Bhojanapalli, David McAllester, and Nati Srebro. Exploring generalization in deep learning. *Advances in neural information processing systems*, 30, 2017.

Jaideep Pathak, Shashank Subramanian, Peter Harrington, Sanjeev Raja, Ashesh Chattopadhyay, Morteza Mardani, Thorsten Kurth, David Hall, Zongyi Li, Kamyar Azizzadenesheli, et al. Fourcastnet: A global data-driven high-resolution weather model using adaptive fourier neural operators. *arXiv preprint arXiv:2202.11214*, 2022.

Maziar Raissi and George Em Karniadakis. Hidden physics models: Machine learning of nonlinear partial differential equations. *Journal of Computational Physics*, 357:125–141, 2018.

Olaf Ronneberger, Philipp Fischer, and Thomas Brox. U-net: Convolutional networks for biomedical image segmentation. In *International Conference on Medical image computing and computer-assisted intervention*, pp. 234–241. Springer, 2015.

Changjian Shui, Qi Chen, Jun Wen, Fan Zhou, Christian Gagné, and Boyu Wang. Beyond $\mathcal{H}$-divergence: Domain adaptation theory with jensen-shannon divergence. *arXiv preprint arXiv:2007.15567*, 2020.

Karen Simonyan and Andrew Zisserman. Very deep convolutional networks for large-scale image recognition. *arXiv preprint arXiv:1409.1556*, 2014.

Alasdair Tran, Alexander Mathews, Lexing Xie, and Cheng Soon Ong. Factorized fourier neural operators. *arXiv preprint arXiv:2111.13802*, 2021.

Tapas Tripura and Souvik Chakraborty. Wavelet neural operator for solving parametric partial differential equations in computational mechanics problems. *Computer Methods in Applied Mechanics and Engineering*, 404:115783, 2023.

Gege Wen, Zongyi Li, Kamyar Azizzadenesheli, Anima Anandkumar, and Sally M Benson. U-fno–an enhanced fourier neural operator based-deep learning model for multiphase flow. *arXiv preprint arXiv:2109.03697*, 2021.

Yan Yang, Angela F Gao, Jorge C Castellanos, Zachary E Ross, Kamyar Azizzadenesheli, and Robert W Clayton. Seismic wave propagation and inversion with neural operators. *The Seismic Record*, 1(3):126–134, 2021.

Chiyuan Zhang, Samy Bengio, Moritz Hardt, Benjamin Recht, and Oriol Vinyals. Understanding deep learning (still) requires rethinking generalization. *Communications of the ACM*, 64(3):107–115, 2021.

A Appendix

A.1 Positional Embedding For Unit Torus

A unit torus $\mathbb{T}^2$ is homeomorphic to the Cartesian product of two unit circles: $S^1 \times S^1$. We can also consider the cartesian product of the embedding of the circle. which produces Clifford torus. The Clifford torus can be defined as

$$\frac{1}{2}S^1 \times \frac{1}{2}S^1 = \left\{ \frac{1}{2}(sin(\theta), cos(\theta), sin(\phi)cos(\phi)) \mid 0 \leq \theta \leq 2\pi, 0 \leq \phi \leq 2\pi \right\}$$

A.2 Sensitivity to Hyper-parameter Selection

Learning Rate →, Depth ↓

Error Rate (Training Set)

Depth	0.01	0.005	0.001	0.0005	0.0001
7	0.4435	0.4188	0.3656	0.483	1.2261
9	0.4435	0.4188	0.3656	0.483	1.2261
11	0.4276	0.3114	0.2503	0.2484	0.6188
13	0.4896	0.2843	0.2249	0.1994	0.5106
15	0.3861	0.2709	0.2339	0.2573	0.449
17	0.3882	0.2847	0.231	0.2761	0.4474

Error Rate (Test Set)

Depth	0.01	0.005	0.001	0.0005	0.0001
7	0.8129	0.8209	0.7625	0.9061	1.8448
9	0.723	0.5907	0.5539	0.6229	1.622
11	0.7094	0.6339	0.6104	0.6402	1.6007
13	0.8946	0.7012	0.5783	0.5964	2.3528
15	0.8195	0.7558	0.6551	0.7019	1.9204
17	0.8244	0.7704	0.6586	0.8074	1.8612

Generalization Gap

Depth	0.01	0.005	0.001	0.0005	0.0001
7	0.3694	0.4021	0.3969	0.4231	0.6187
9	0.2795	0.1719	0.1882	0.1399	0.396
11	0.2818	0.3225	0.36	0.3918	0.9819
13	0.405	0.4169	0.3534	0.3971	1.8421
15	0.4334	0.4849	0.4212	0.4446	1.4714
17	0.4362	0.4858	0.4275	0.5313	1.4138

Figure 4: Result of sensitivity of $U\text{-}NO^{\dagger}$ to learning rate and number of stacked non-linear operator (depth) used. All models are trained on the dataset of the Darcy Flow equation with resolution 211×211 following the training protocol described in 4.4. Models for each of the configuration is trained three times and the average error rate (in %) is reported. We can notice that except for a very high (≥ 0.01) or very low (≤ 0.0001) learning rate, $U\text{-}NO^{\dagger}$ achieves low error rate at every other configurations (**error rate achieved by *FNO* is 0.85**). We also note that at all the high-performing hyper-parameter configuration setting *U-NO* has low generalization gap.

Table 5: Number of Parameters in $U\text{-}NO^{\dagger}$ models at different depth. We observe $U\text{-}NO^{\dagger}$ architecture can efficiently learn large number of parameter (**25** times of the *FNO*) from very limited training data (only 1500 simulations) and can perform reasonably (See Table. 4)

Depth	7	9	11	13	15	17
#Parameters ($\times 10^6$)	5.3	8.3	9.6	18.5	22.8	27.8

A.3 *FNO* with Skip Connection

Table 6: Performance of vanilla 2D *FNO* equipped with skip connection on Navier-Stokes equations described in Section 4.5 along with memory requirement during training. The result of 2D *FNO* is reported again for comparison. We notice that skip connection alone does not improve the performance of *FNO*.

Models *U-NO*	**Memory Requirement** (MB)	$\nu = 1\text{e}{-3}$ $N = 2400$	$\nu = 1\text{e}{-4}$ $N = 6000$	$\nu = 1\text{e}{-5}$ $N = 6000$	$\nu = 1\text{e}{-6}$ $N = 6000$
FNO w. skip con.	13.14 MB	0.011	0.074	0.075	**0.049**
FNO	**13.03 MB**	**0.009**	**0.072**	**0.074**	0.052

A.4 Spatial Memory

The memory requirements to learn the operator $w|_{(0,1)^2 \times [0,10]} \rightarrow w|_{(0,1)^2 \times (10,11]}$ during back-propagation for the Navier-Stokes problem are shown in Table 7. On average, for various tested resolutions, *U-NO* with a contraction (and expansion) factor of $\frac{1}{2}$ requires 40% less memory than *FNO* during training. This makes *U-NO* and its variants more suitable for problems where high-resolution data are crucial, e.g., weather forecasting model (Pathak et al., 2022).

Table 7: Memory requirements (in MB) for a single training instance of the Navier-Stokes equations for different grid resolutions. All models have seven non-linear integral operator layers.

Spatial Resolution	*FNO*	*U-NO*	*U-NO*†
64×64	13.0	16.8	11.3
128×128	76.1	67.3	45.4
256×256	304.5	269.0	181.5
512×512	1218.0	1076.0	726.0
1024×1024	4872.0	4304.0	2990.9

A.5 Zero-Shot super resolution on 3D Spatio-Temporal Data

Table 8: Zero-shot super resolution result on 3D spatio-temporal Navier Stocks equation. The 3D *FNO* is not resolution invariant in the time domain and due the specific construction can not process data at different temporal resolution. But *U-NO* is resolution invariant both in time and spatial domain.

	Spatial Res. \ Temporal Res.	fps = 1	fps = 1.5	fps = 2	fps = 3
U-NO	s=64	5.10	17.43	19.39	20.32
	s=128	6.34	17.61	19.56	20.62
	s=256	8.16	17.86	19.94	20.83

A.6 Superior Convergence Rate

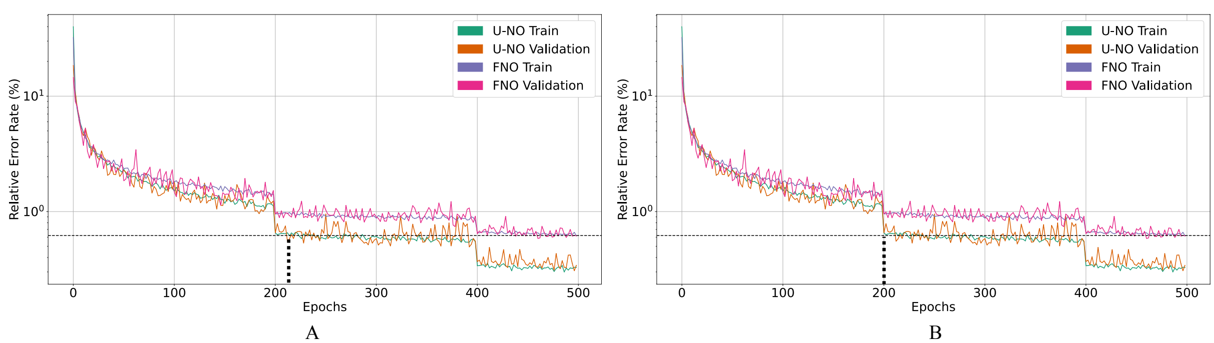

Figure 5: The training and test set error rate (in % on log scale) of *U-NO* and *FNO* for Navier-Stokes equation with viscosity $10e^{-3}$, (A) models performing $2D$ spatio-temporal convolution (B) models performing $3D$ spatial covolution. We can notice what *U-NO* converges much faster than *FNO*. The final test set error rate for *FNO* after **500** epochs is achieved only after around **200** epochs by *U-NO* and continues to improve on the error rate.

B Training Memory Requirement for 2D *U-NO* at Different Depths

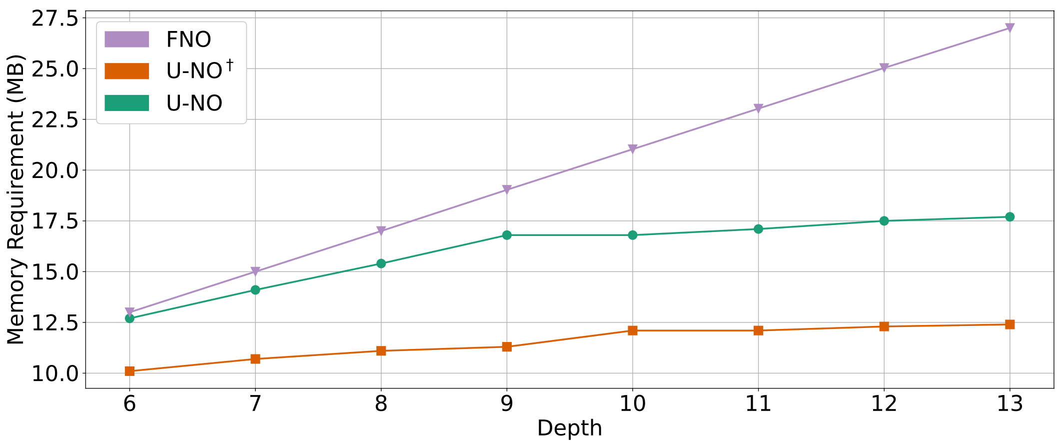

Figure 6: Memory requirements (in MB) for a single training instance of the Navier-Stokes equation during back-propagation on input and outputs of resolution 64×64. Number of stacked non-linear operators is varied and the additive memory requirement of *U-NO* architectures for deeper models are negligible compared to *FNO* model. For *U-NO*† the addition of **7** stacked non-linear integral operator increases the memory requirement by only **2.5 MB**